Chinese Journal of Mechanical Engineering

ORIGINAL ARTICLE

Open Access

Relations of Microstructural Attributes and Strength-Ductility of Zirconium Alloys with Hydrides

Chao Fang[1], Xiang Guo[1,2*], Jianghua Li[3] and Gang Chen[4*]

Abstract

As the first safety barrier of nuclear reactors, zirconium alloy cladding tubes have attracted extensive attention because of its good mechanical properties. The strength and ductility of zirconium alloy are of great significance to the service process of cladding tubes, while brittle hydrides precipitate and thus deteriorate the overall performance. Based on the cohesive finite element method, the effects of cohesive strength, interfacial characteristics, and hydrides geometric characteristics on the strength and ductility of two-phase material (zirconium alloy with hydrides) are numerically simulated. The results show that the fracture behavior is significantly affected by the cohesive strength and that the overall strength and ductility are sensitive to the cohesive strength of the zirconium alloy. Furthermore, the interface is revealed to have prominent effects on the overall fracture behavior. When the cohesive strength and fracture energy of the interface are higher than those of the hydride phase, fracture initiates in the hydrides, which is consistent with the experimental phenomena. In addition, it is found that the number density and arrangement of hydrides play important roles in the overall strength and ductility. Our simulation provides theoretical support for the performance analysis of hydrogenated zirconium alloys during nuclear reactor operation.

Keywords Zirconium alloy, Hydride, Strength and ductility, Cohesive finite element method, Microcrack initiation and propagation

1 Introduction

Zirconium alloys are widely used in fuel cladding tubes in nuclear reactors. They attract more attention than other materials because of a series of advantages such as excellent thermal conductivity, corrosion resistance, and extremely low neutron absorption cross section [1, 2]. Fuel cladding wraps the fissile radioactive uranium fuel pellets, acts as the first barrier against the release of radioactive elements, and directly contacts the coolant [3, 4]. As we all know, the integrity of structural materials is usually very crucial [5]. During the operation of the reactors, corrosion reactions occur at the interface between the coolant and the nuclear fuel cladding, and hydrogen atoms released by this process diffuse into the zirconium alloys [6]. The solid solubility of hydrogen in zirconium alloys is relatively low, and it remains solid solute state till reaching the solid solubility. When the solid solubility is exceeded, brittle hydrides precipitate in the zirconium alloys and then they deteriorate the mechanical properties of cladding materials [7, 8]. It is well known that

*Correspondence:
Xiang Guo
xiangguo@tju.edu.cn
Gang Chen
agang@tju.edu.cn
[1] School of Mechanical Engineering, Tianjin University, Tianjin 300354, China
[2] Tianjin Key Laboratory of Nonlinear Dynamics and Control, Tianjin 300072, China
[3] State Key Laboratory of Nonlinear Mechanics, Institute of Mechanics, Chinese Academy of Sciences, Beijing 100190, China
[4] School of Chemical Engineering and Technology, Tianjin University, Tianjin 300072, China

hydrogen embrittlement is one of the most important causes for the fracture and premature failure of nuclear fuel cladding tubes during the operation process of nuclear reactors. Therefore, the effects of hydrides on the strength and ductility of hydrogenated zirconium alloys are important to evaluate the structural integrity.

It was found that the hydrides might have defects because the occurrence of hydrogenated α-Zr involves a large volume expansion, about 17% of a unit cell [9]. In an oxygen-rich environment, local overabsorption and thermal transport of hydrogen leads to hydride blisters [10, 11]. The emergence of these hydride blisters is usually related to the stress concentration in the nuclear fuel cladding, and cracks initiate at these hydride blisters [12]. The phenomenon that hydrides induce crack propagation in the zirconium alloys is often referred to as the delayed hydride cracking, and the relevant study is crucial to the integrity and reliability of nuclear fuel cladding [13–15].

In the operation of nuclear reactors, the influences of hydride phase on the hydrogenated zirconium alloys are not negligible. In order to investigate the adverse effects of hydrides on the overall ductility, fracture toughness, and service life of zirconium alloys, many researchers have carried out extensive study. On the one hand, due to the brittleness of the hydrides, experimental studies have revealed that the mechanical properties of zirconium alloys are degraded significantly. Kim et al. [16] found that the degradation of the performance depended not only on the orientation of the hydrides but also on the concentration of the hydrides in the cladding tubes. Zhang et al. [17] studied the effects of hydrogen concentration and temperature on the fatigue crack initiation and propagation in the zirconium alloy by in-situ scanning electron microscopy. However, due to the limitation of experiments, it is difficult to accurately repeat the key factors such as the geometric characteristics of hydride phase. On the other hand, numerical simulation is an effective approach to study the fracture behavior of hydrogenated zirconium alloys. For instance, Tseng et al. [18] studied the crack through hydrides in the fuel cladding by the finite element method, and found that long hydrides and double radial hydrides had significant influences. By means of the cohesive finite element method (CFEM), Fang et al. [19] numerically simulated the ductile fracture process in hydrogenated zirconium alloy under different stress states and analyzed the influences of geometric characteristics of hydrides. However, the previous numerical simulation lacks the attention to the effects of the hydrides on the strength and ductility of cladding, and so far, theoretical elaboration of experimental phenomenon is far from enough. Therefore, the numerical simulation is used in this work to clarify the above problems comprehensively.

Stemming from the principle of virtual work, the extended finite element method (XFEM) [20], the isogeometric analysis (IGA) combining with the XFEM (known as extended IGA (XIGA)) [21, 22], and the CFEM [23–25] have been widely used in investigating the fracture processes. The former two have some difficulties in modeling spontaneous multi-crack initiation, branching, and coalescence, while they are often used to study single crack propagation [26]. Compared with them, the CFEM has obvious advantages. Specifically, it can effectively simulate the propagation of pre-cracks and also the initiation and propagation of multiple microcracks in the fracture process. Therefore, the CFEM is adopted in this study.

In this paper, microstructural attributes include fracture characteristics of the zirconium alloy and hydrides, interfacial characteristics, and geometric characteristics of hydrides. Based on the CFEM, we simulate the fracture behavior of hydrogenated zirconium alloys and explore the correlation between the microstructural attributes, and overall strength and ductility.

2 Numerical Framework

The strength and ductility of structural materials are crucial to evaluate the integrity and reliability of engineering structures [27–29]. In this study, in order to clarify the effects of hydrides on the strength and ductility of hydrogenated zirconium alloys, idealized microstructures are presented in Section 2.1. The hydrides are generally in microns and more brittle, while the zirconium alloys are more ductile. Therefore, a big gap exists between the mechanical properties of hydrides and zirconium alloy. To study the performance of the above two-phase material, the plastic constitutive laws of two phases are given in Section 2.2, and the bilinear traction-separation law is described in Section 2.3.

2.1 Idealized Microstructures

This study aims at a rectangular sample ($400 \times 300\ \mu m^2$) of zirconium alloy with hydride(s). The damage evolution in the two-phase material is numerically simulated by the CFEM. The involved element types include solid element and cohesive element, and cohesive elements are inserted between two adjacent solid elements. According to the distribution locations, the cohesive elements in the zirconium alloy matrix are referred to as Zr-Zr elements, those in the hydride phase are H-H elements, while those between the zirconium alloy and hydride are Zr-H elements (i.e., interface elements). Figure 1 shows a typical microstructure (Model-1), in which the red region is the hydride phase (length L_h: 200 μm, width L_b: 30 μm) and the green region is the zirconium alloy. The yellow region represents the Zr-Zr

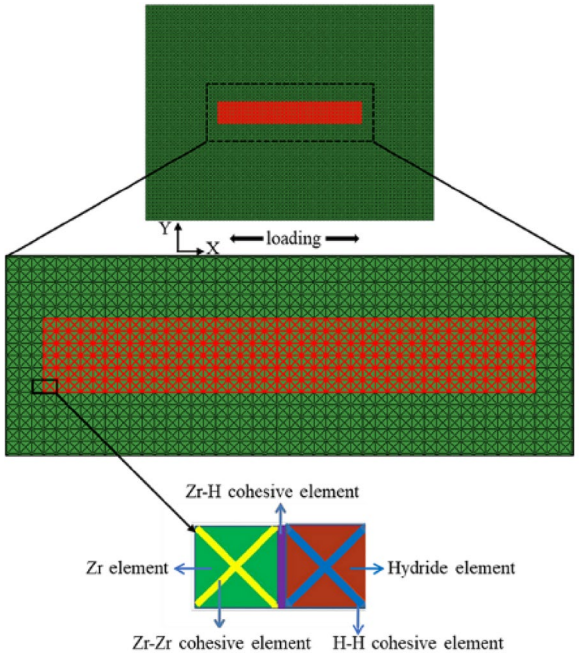

Figure 1 Microstructure of Model-1

elements, the blue region represents the H-H elements, while the purple region represents the Zr-H elements.

Among multiple categories of solid and cohesive elements, the linear triangular plane stress solid element and the two-dimensional four nodes cohesive element are used. Displacement boundary conditions are applied to the left and right boundaries of the sample. The upper and lower boundaries are unconstrained. Simulation is carried out by the finite element software package ABAQUS [30].

The number density, spacing, and arrangement of hydrides are important to the fracture process of hydrogenated zirconium alloys. In order to facilitate subsequent analysis, nine microstructures are designed and then divided into three series according to the arrangement of hydrides, as illustrated in Figure 2:

(i) One-hydride series (series A) including microstructure A1 (Figure 2a), A2 (Figure 2b), and A3 (Figure 2c). In A1, the hydride is along the tensile direction; in A2, it is perpendicular to the tensile direction; in A3, it is at an angle of 45° with the tensile direction.

(ii) Two-hydride series (series B) including microstructure B1 (Figure 2d), B2 (Figure 2e), B3 (Figure 2f), and B4 (Figure 2g). B1 contains two coaxial hydrides along the tensile direction; B2 contains two uncoaxial hydrides along the tensile direction; B3 contains two hydrides perpendicular to the tensile direction; B4

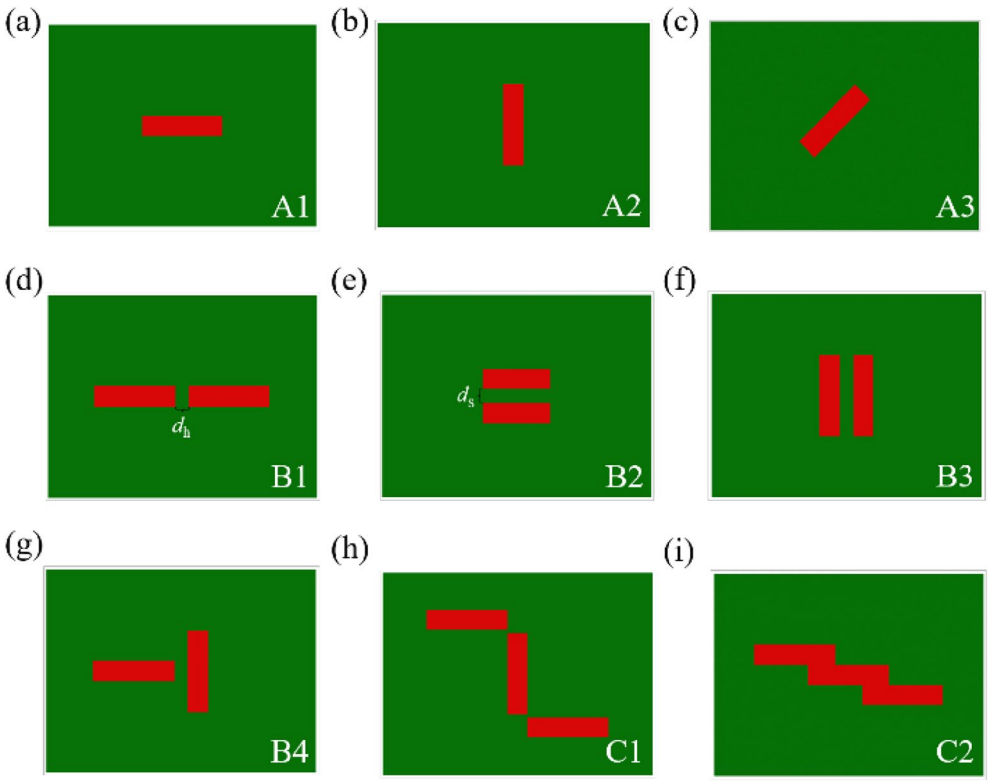

Figure 2 Nine idealized microstructures: **a** A1, **b** A2, **c** A3, **d** B1, **e** B2, **f** B3, **g** B4, **h** C1, and **i** C2

Table 1 Elastoplastic research of zirconium alloys

Literature	Study object	Study methods	Main content
Liu et al. [31]	Zircaloy-4 alloy cladding	Experiment	Crystal orientation & mechanical properties
Chen et al. [32]	Zirconium alloy tubes	Experiment	A series of uniaxial and multiaxial ratchet test
Murty et al. [33]	Zircaloy tubes	Experiment	An automatic technology to measure mechanical and fracture properties
Nilsson et al. [34]	Zircaloy-4 cladding	Experiment as well as simulation	Evaluation on effects of hydride based on the finite element method

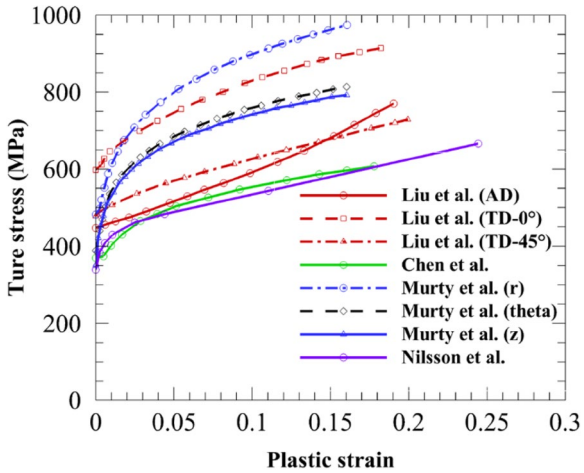

Figure 3 True stress versus plastic strain of zirconium alloy

contains one hydride along the tensile direction and one perpendicular to it.

(iii) Three-hydride series (series C) including microstructure C1 (Figure 2h) and C2 (Figure 2i). C1 has two hydrides along the tensile direction and one perpendicular to it; C2 has three overlapped hydrides along the tensile direction.

In series A, series B, and series C, the length and width of hydrides are 120 μm and 30 μm, respectively, except that in microstructure A3, they are 116.67 μm and 31.82 μm. For the two hydrides in microstructures B1–B4, both the spacing along the tensile direction d_h and the spacing perpendicular to the tensile direction d_s are 20 μm.

2.2 Plastic Constitutive Laws

The plastic constitutive law of zirconium alloy should be specified. Table 1 lists the available results from tensile tests and Figure 3 depicts the true stress versus the plastic strain. Here, a moderate plastic constitutive law (theta direction) [33] is adopted for the zirconium alloy. So far, there are relatively few results on the plastic constitutive law of hydrides. Here, the results in Ref. [35] is adopted for the hydrides.

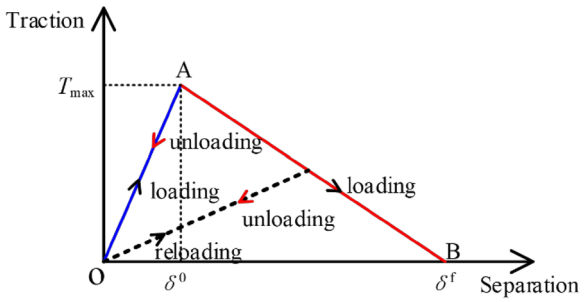

Figure 4 Bilinear traction-separation law

2.3 Cohesive Finite Element Method

The behavior of cohesive elements can be characterized by the traction-separation laws [36, 37]. A bilinear traction-separation law can clearly describe a linear elastic stage of cohesive elements and a linear softening stage after reaching the peak, as shown in Figure 4. When an effective separation δ reaches δ^0, the traction reaches cohesive strength T_{max} [23]. When δ is smaller than δ^0, the loading and unloading process is fully reversible. When δ is larger than δ^0, the loading and unloading process becomes irreversible. When δ reaches a failure separation δ^f, the traction reduces to zero, the cohesive element fails, and thus the microcrack initiates. In the mixed-mode situation, the damage initiation criterion is very important. When it is satisfied, the material begins to degrade. The criterion adopted in this study is the quadratic nominal stress criterion (Quads), i.e., the damage initiation occurs when

$$\left\{\frac{\langle t_n\rangle}{t_n^0}\right\}^2+\left\{\frac{t_s}{t_s^0}\right\}^2=1, \tag{1}$$

where t_n and t_s are the traction in the normal and shear directions, respectively; $\langle t_n\rangle = t_n$ when $t_n > 0$, and $\langle t_n\rangle = 0$ when $t_n \le 0$; t_n^0 and t_s^0 represent the maximum nominal stress in mode I (opening mode) and mode II (sliding mode) failure, respectively.

In the two-dimensional case, G_{coh} (fracture energy) is the energy required for failure of cohesive element per unit length, and its value is equal to the area of ΔOAB

enclosed by two segments and X axis in Figure 4. It can be calculated as:

$$G_{\mathrm{coh}} = \int_0^{\delta^{\mathrm{f}}} T(\delta)\mathrm{d}\delta = 0.5 T_{\max}\delta^{\mathrm{f}}, \tag{2}$$

where T is the effective traction [23].

Table 2 shows the parameters input to the solid and cohesive elements. As listed in the table, the cohesive strength of Zr-Zr and H-H elements are taken as n_{Zr} times of the yield stress of zirconium alloy and n_{H} times of the yield stress of hydride, respectively. In addition, the fracture toughness (K_{C}) of zirconium alloy was measured to be 40 MPa$\sqrt{\mathrm{m}}$ [39] and that of hydride 3.3 MPa$\sqrt{\mathrm{m}}$ [40]. Therefore, the fracture energy of Zr-Zr elements can be calculated as 16508 J·m^{-2} by the formula ($\phi_{\mathrm{n}} = K_{\mathrm{C}}^2(1-\nu^2)/E$), and that of H-H elements 89 J·m^{-2}. Unless otherwise stated, for the Zr-H elements, the cohesive strength and fracture energy are taken as the averages of Zr-Zr and H-H elements [23, 24]. In order to facilitate follow-up discussion, the combination of n_{Zr} and n_{H} is denoted n_{Zr}-n_{H} in this study.

3 Results and Discussion

In this section, we carry out the qualitative comparisons of simulated results with experiments, and then explore the influences of the microstructural attributes ((i) the cohesive strength of each phase, (ii) the interfacial characteristics (cohesive strength and fracture energy), and (iii) the geometric characteristics (number density, spacing, and arrangement) of hydrides) to the strength and ductility of hydrogenated zirconium alloys.

3.1 Comparisons with Experimental Phenomena

Comparisons between simulated results and the experimental phenomena are shown in Figure 5. Specifically, in order to verify our numerical framework by comparing with the tensile fatigue experimental phenomenon in Figure 5a [41], another microstructure with a slender hydride is designed and shown in Figure 5b. It is evident that when n_{Zr}-n_{H} is 1.8-1.2, the fracture morphology and the blunting characteristics around crack tips are quite consistent with the experiment. The number density of microcracks is larger than that of microcracks in the experiment, which might lie in different load conditions and stress states. Furthermore, Figure 5c illustrates the maximum shear strain in the hydrogenated zirconium alloy in the macroscopic tensile test of Wang et al. [42], while Figure 5d shows our equivalent plastic strain of Model-1 (n_{Zr}-n_{H} is 1.8-1.2) before microcrack initiation. As seen in Figure 5c and d, the region with high strain is concentrated both at the interface and in the zirconium alloy matrix, and our simulation in a qualitative agreement with the experimental strain distribution characteristics. Therefore, the above two comparisons (fracture morphology, strain distribution characteristics of two-phase material) demonstrate that our numerical framework is reliable. Furthermore, n_{Zr}-n_{H} values can be taken as 1.8-1.2 except in Section 3.2.

3.2 Influences of Cohesive Strength

The initiation and propagation of microcracks depend heavily on the damage initiation and evolution of cohesive elements. Therefore, in this section, we conduct parametric study on the cohesive strength of zirconium alloy and hydrides to explore their influences on the overall fracture process. On the one hand, Figure 6a shows the stress-strain curves for Model-1 when n_{Zr} is 1.5, 1.8, and 2, while n_{H} is 1.2. It is evident that with the increase in n_{Zr}, both the overall strength and ductility increase significantly. Equivalently, they are very sensitive to the cohesive strength of Zr-Zr elements. On the other hand, Figure 6b depicts the stress-strain curves for Model-1 when n_{H} is 1.1, 1.3, and 1.5, while n_{Zr} is 1.8. It can be seen that the overall strength and ductility increase modestly with the increase in n_{H}.

3.3 Influences of Interfacial Characteristics

Formers' studies revealed that when the strength and ductility of matrix and inclusion phase differed a lot, debonding would occur at the interface, which would promote crack propagation and even rapid failure [23, 43, 44]. Therefore, the influences of the fracture characteristics of interface elements (Zr-H elements) on the strength and ductility of Model-1 (shown in Figure 1)

Table 2 Constitutive parameters for bulk and cohesive elements

	Yield stress (MPa)	Elastic modulus (GPa)	Poisson's ratio	Cohesive strength (MPa)	Fracture energy (J·m^{-2})
Zr [18, 38]	389	87	0.32	–	–
Hydride [35]	400	110	0.32	–	–
Zr–Zr	–	–	–	$389\times n_{\mathrm{Zr}}$	16508
H–H	–	–	–	$400\times n_{\mathrm{H}}$	89
Zr–H	–	–	–	$(389\times n_{\mathrm{Zr}} + 400\times n_{\mathrm{H}})/2$	8298

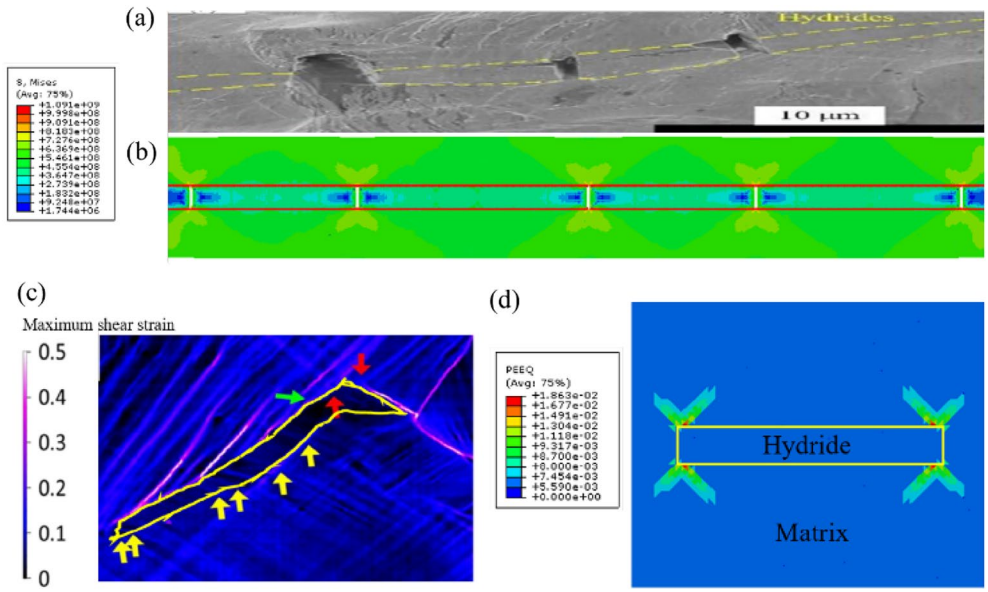

Figure 5 Comparison between the simulated results and experiments: **a** Experimental morphology (Reprinted from Ref. [41] with permission from Elsevier Science), **b** Simulated morphology, **c** Experimental strain distribution (Reprinted from Ref. [42] with permission from Elsevier Science), **d** Simulated equivalent plastic strain distribution

are studied. Four categories of interfaces are introduced according to the fracture characteristics of Zr-H elements:

(i) Interface I – Its cohesive strength and fracture energy are half of the corresponding values of H-H elements;
(ii) Interface II – Its cohesive strength and fracture energy are the same as those of H-H elements;
(iii) Interface III – Its cohesive strength and fracture energy are the corresponding averages of Zr-Zr and H-H elements;
(iv) Interface IV – Its cohesive strength and fracture energy are the same as those of Zr-Zr elements.

Note that the cohesive strength and fracture energy of Zr-H element gradually increase from interface I to IV. Equivalently, the fracture characteristics of interface I are the worst, while those of interface IV are the best.

Figure 7 shows the stress-strain curves for Model-1 with the four categories of interfaces. The overall strength and ductility associated with interface I are superior to those associated with the other three cases. It can be seen that the overall stress-strain curve is relatively smooth in the case of interface I, and the Zr-H element gets damaged first and then a microcrack initiates, and the entire microstructure fails eventually with the tensile deformation. The overall strength and ductility associated with interface II, III, and IV are essentially the same. In all three cases, the stress-strain curves have obvious fluctuation, as illustrated in the zoomed box in Figure 7.

In order to further explore the influences of interfacial characteristics, Figure 8 shows the fracture morphologies of Model-1 with four categories of interfaces. Although the ratio of interface elements to the total cohesive elements is as low as 0.32%, the interfacial characteristics have great influences on the overall performance. As illustrated in Figure 8a, in the case of interface I, the microcracks occur at the interface, and then continuously and steadily propagate in the zirconium alloy perpendicular to the tensile direction till the eventual failure. As shown in Figure 8b, in the case of interface II, the microcracks initiate at the interface and in the mid-span of the hydride as the cohesive strength and fracture energy of the interface elements are the same as those of the hydride. As depicted in Figure 8c and d, in the cases of interface III and IV, the cohesive strength and fracture energy of the interface elements are larger than those of the hydride, so that microcracks occur both near to the interface and in the mid-span of the hydride, which is different from the phenomenon in Figure 8b. Note that the fracture morphologies associated with interface III and IV are consistent with the experimental phenomenon that the fracture initiates in the hydrides of hydrogenated zirconium alloys [12, 41]. In general, in the case of interface II, both the Zr-H and H-H elements get damaged first, while in the cases of interface III and IV, damage initiates only in the H-H elements. In short, once the

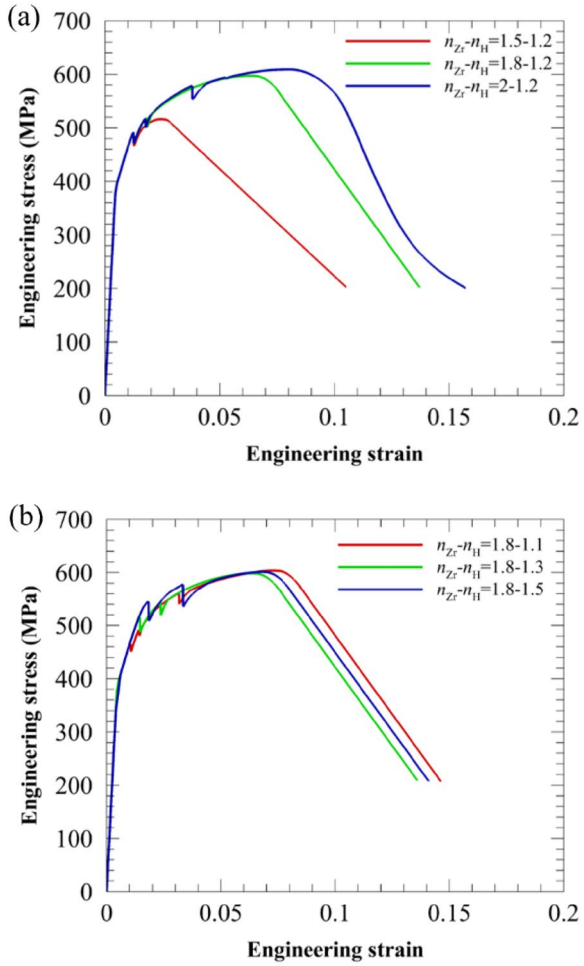

Figure 6 Engineering stress-strain curves for Model-1: **a** n_{Zr} = 1.5, 1.8, and 2, while n_H = 1.2, **b** n_H = 1.1, 1.3, and 1.5, while n_{Zr} = 1.8

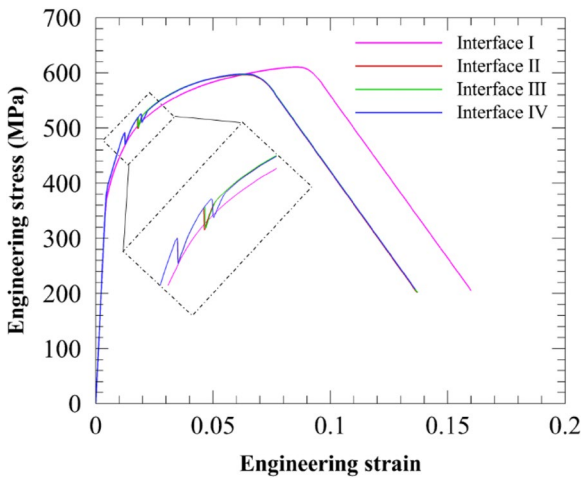

Figure 7 Engineering stress-strain curves for Model-1 with the four categories of interfaces (n_{Zr}–n_H = 1.8-1.2)

hydride is present, no matter of categories of interface, the microcrack initiates either in the hydride or at the interface, which implies larger influences of the hydride on the microcrack initiation.

3.4 Influences of Geometric Characteristics of Hydrides

The geometric characteristics of hydride phase cannot be controlled precisely in the experiments. Some studies [18, 19] have focused on the effects of geometric characteristics (size, arrangement, quantity, and spacing) of hydrides on the fracture behavior of hydrogenated zirconium. Furthermore, to explore the strength and ductility of hydrogenated zirconium alloys, the effects of geometric characteristics (number density, spacing, and arrangement) of hydrides need to be studied in details.

Studies have shown that when the hydride width L_b remains 30 μm, its length L_h varies from 100 μm to 200 μm [45]. This motivates us to study the effects of the number density of hydrides while keeping the same volume fraction of hydrides. In Figure 2a, the model with a hydride (the length L_h: 200 μm, the width L_b: 30 μm) is Model-1. In Figure 2d and 2e, the models with two coaxial and uncoaxial hydrides (the length L_h: 100 μm, the width L_b: 30 μm) are denoted as Model-2 and Model-3, respectively. The distance d_h and d_s are kept at 60 μm.

Figure 9 shows the stress-strain curves of microstructures with the same volume fraction but the different number density of hydrides. On the one hand, both the strength and ductility of Model-2 are the best, while those of Model-3 are the worst. Specifically, the tensile strength of Model-2 is 598 MPa and the failure strain is 0.07; the tensile strength of Model-3 is 529 MPa and the failure strain is 0.043. Equivalently, the strength of the specimen with the coaxial hydrides is 1.13 times of that with the uncoaxial ones, and the ductility of the former is 1.62 times of that of the latter. It can also be found that when the same volume fraction of hydrides is remained, the microstructure with two hydrides along the tensile direction is slightly more ductile than that with one hydride along the tensile direction. More importantly, the coaxial hydrides lead to much better overall strength and ductility than the uncoaxial ones. On the other hand, no matter in Model-1, Model-2, or Model-3, the microcrack initiation location is close to the interface. Note that in Model-2, the first and second microcracks initiate close to the interfaces near to the tensile ends. Subsequently, the third and fourth microcracks initiate close to the interfaces at the middle position of the microstructure. However, in Model-1 and Model-3, the first and second microcracks initiate near to the interface, and then the third microcrack occurs in the mid-span of each hydride. From the above results, it can be inferred that the

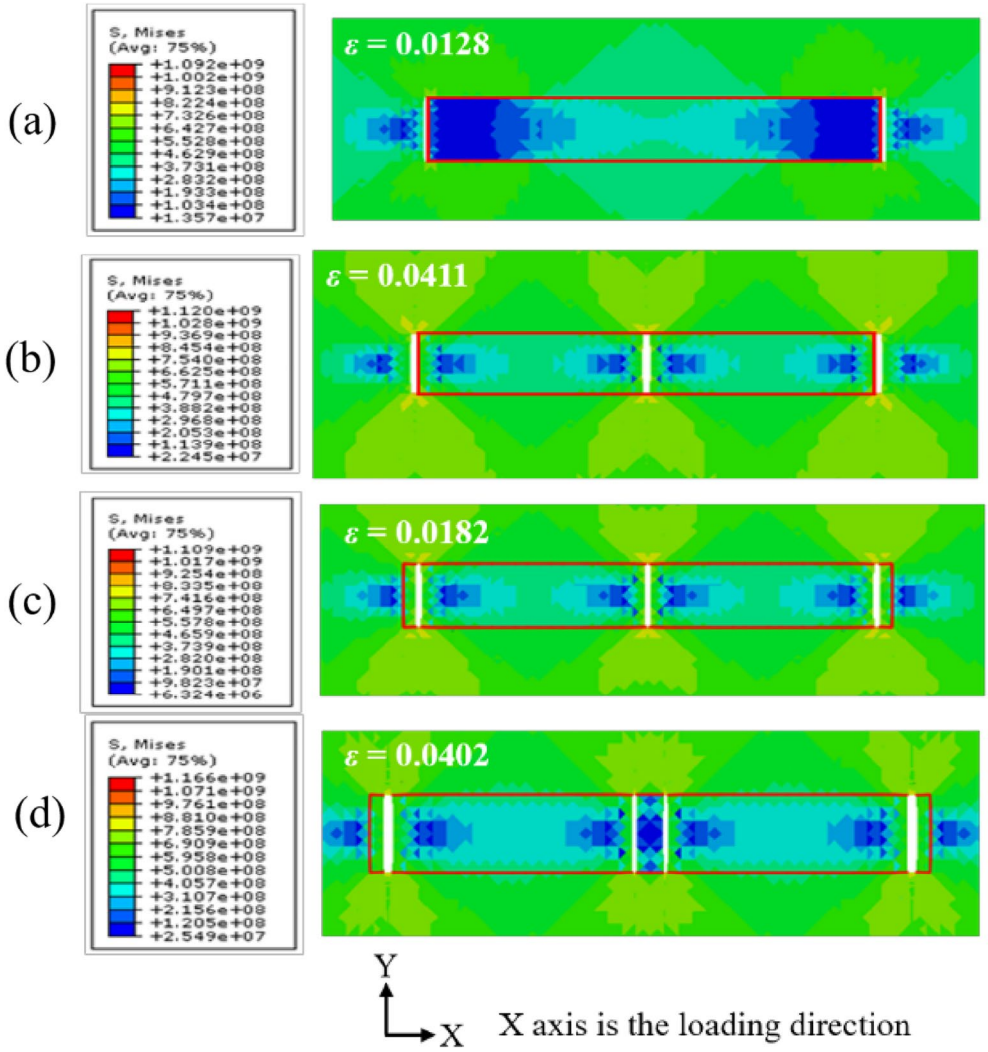

Figure 8 Fracture morphologies of the microstructure with four categories of interfaces: **a** Interface I, **b** Interface II, **c** Interface III, **d** Interface IV (stress in Pa)

specimens with more coaxial hydrides usually have superior performance than those with more uncoaxial ones.

Figure 10 shows the stress-strain curves when the spacing d_h and d_s vary in a microstructure containing two hydrides (L_h: 120 μm, L_b: 30 μm). It can be seen that when the d_h changes from 20 μm to 80 μm, the strength and ductility of the microstructure are improved modestly. When the d_s varies from 20 μm to 80 μm, the overall strength and ductility almost coincide.

Figure 11 shows the stress-strain curves of the microstructures in series A. It can be seen that the arrangement of hydride has obvious influences on the overall performance. Specifically, the strength and ductility of the microstructures with the hydride along the tensile direction are much better than those of the microstructures with the hydride perpendicular to it. This is also consistent with the experimental finding of Li et al. [41] that the radial hydrides perpendicular to the tensile direction are easier to lead to the overall fracture than the circumferential ones. Furthermore, there are three microcracks through the hydride in microstructure A1 and two through the hydride in A2, while the microcracks in A2 are much longer than those in A1. It is noteworthy that in A3, microcracks are also perpendicular to the tensile direction. With the tensile deformation, many microcracks initiate close to the interfaces and then propagate into the matrix phase till the eventual failure.

Figure 12 depicts the stress-strain curves of the four microstructures in series B. It is evident that among the four arrangements, microstructure B1 has the best

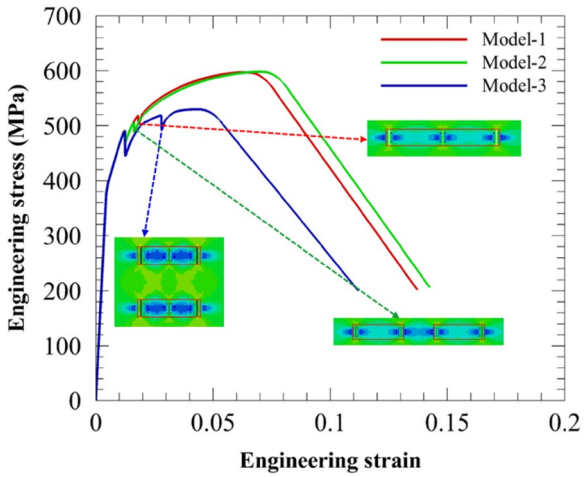

Figure 9 Engineering stress-strain curves of microstructures with the same volume fraction but the different number density of hydrides

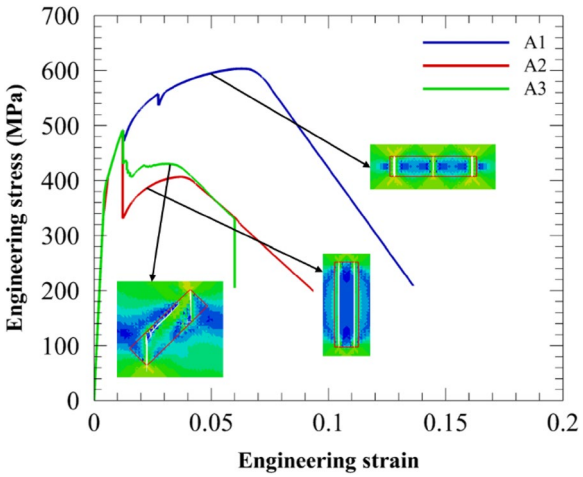

Figure 11 Engineering stress-strain curves of the microstructures in series A

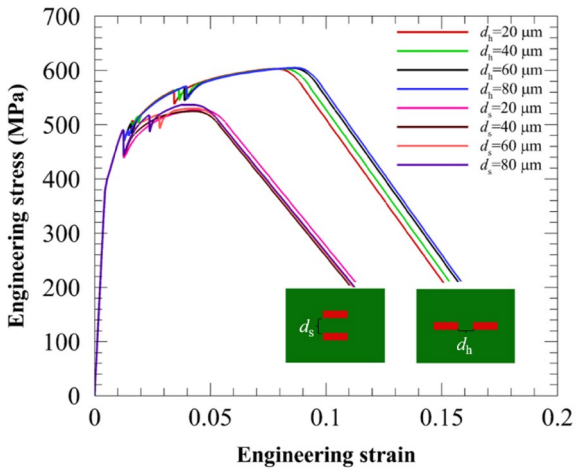

Figure 10 Engineering stress-strain curves when the spacing d_h and d_s of two hydrides change

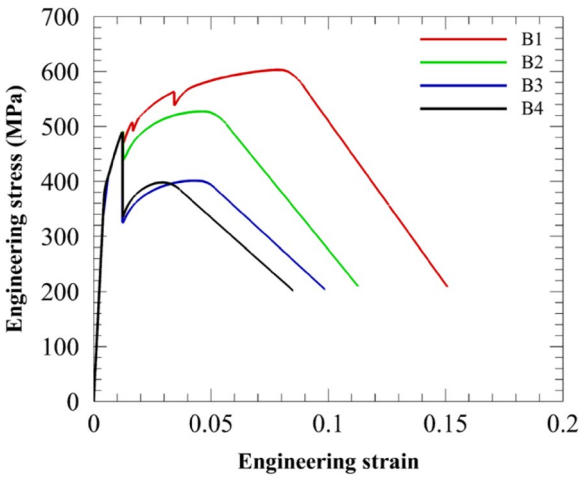

Figure 12 Engineering stress-strain curves of the microstructures in series B

strength and ductility, and B3 and B4 are relatively weaker, while B4 has the worst ductility. Specifically, when they are along the tensile direction, the coaxial hydrides lead to the better overall performance than the uncoaxial ones. Equivalently, the overall performance is tremendously deteriorated when the hydrides are perpendicular to the tensile direction.

Figure 13a–d shows the fracture morphologies of four microstructures (B1, B2, B3, and B4) in series B. In Figure 13a, three microcracks occur in each hydride. The first microcrack initiates close to the interfaces near to the tensile ends, the second at the interface on the other side, and the third in the mid-span of each hydride. In Figure 13b, two microcracks initiate in each hydride and also close to the interfaces. In Figure 13c, a microcrack initiates in each hydride and also close to the interface. In Figure 13d, a microcrack initiate not in the left hydride but in the right one and it is close to the interface. Again, this reflects our finding that the hydride perpendicular to the tensile direction has larger influences on the overall performance than that along it.

The hydride interconnection phenomenon, as shown in microstructure C1 (Figure 2h) and C2 (Figure 2i), extensively exists in the experimental observations [46], so it is interesting to investigate the fracture behavior of the microstructures in series C. On the one hand, for C1, Figure 14a shows the stress concentration around the nearby vertex of the hydrides. Subsequently, as

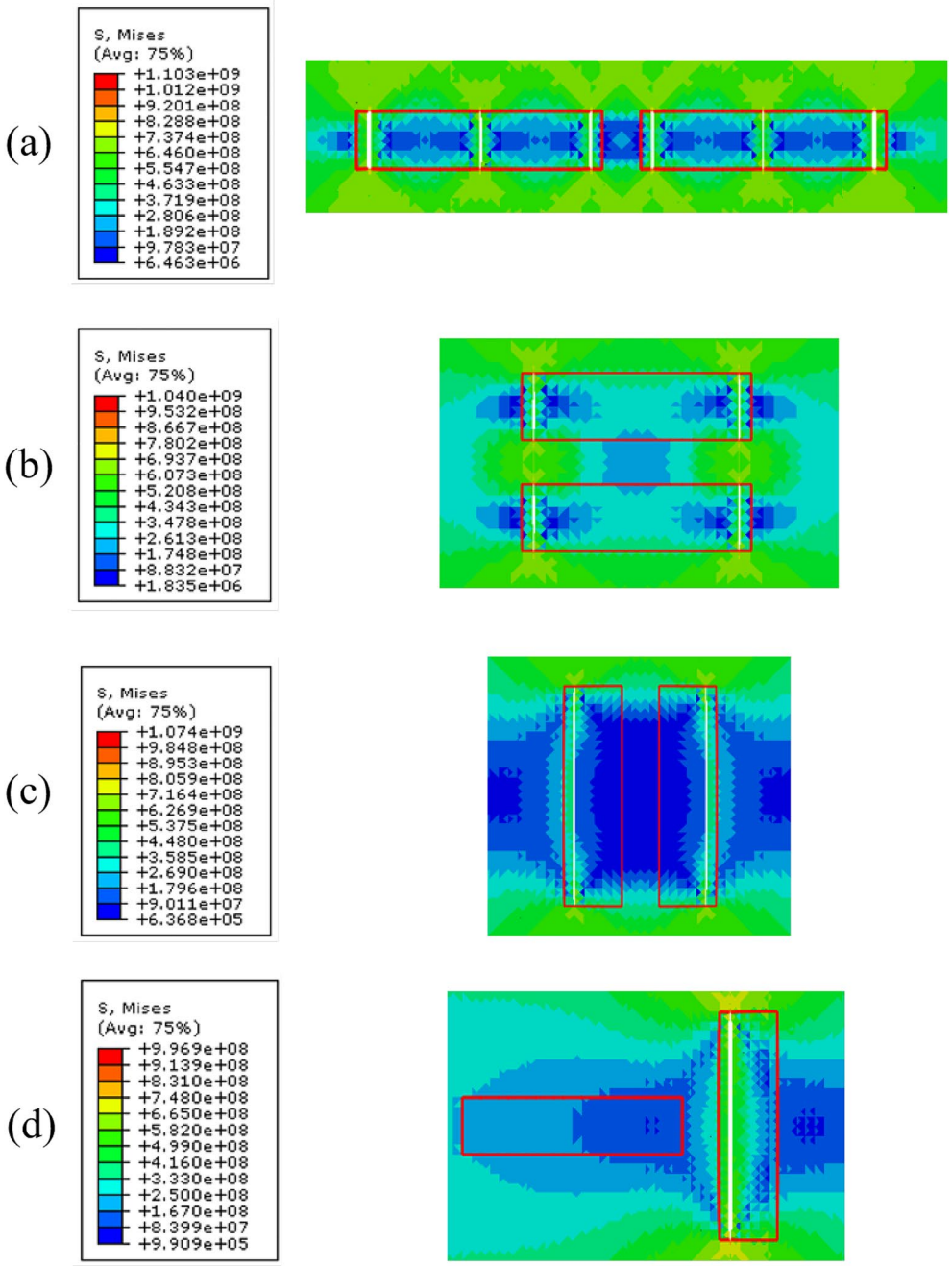

Figure 13 Fracture morphologies of **a** microstructure B1, **b** B2, **c** B3, and **d** B4 (stress in Pa)

shown in Figure 14b, bridging occurs in the stress concentration regions around those vertices. In these regions, crack deflection occurs, which is consistent with the finding in Refs. [47, 48]. On the other hand, for C2, Figure 14c shows the effects of overlapped hydrides on the fracture morphology. The microcrack initiates at the laps and then propagates till C2 fails.

4 Conclusions

The integrity of zirconium cladding tubes is crucial to the safe operation of nuclear reactors. In this paper, the fracture behavior of two-phase material composed of zirconium alloy and hydride(s) is analyzed based on the two-dimensional cohesive finite element method. The effects of microstructural attributes on the strength and

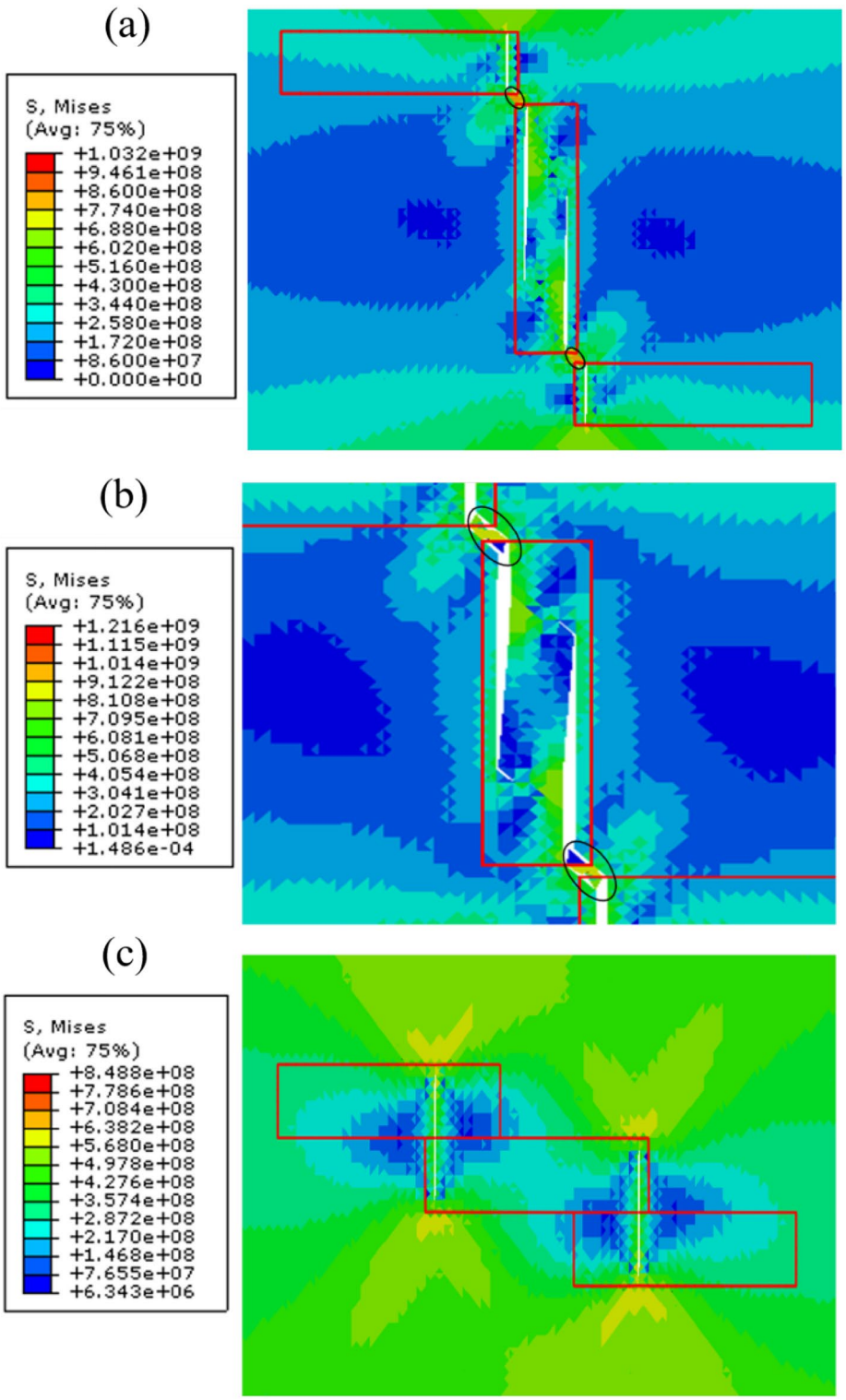

Figure 14 Fracture morphologies of the microstructures in series C: **a** Microcracks and stress concentration in C1, **b** Bridging in C1, **c** Microcracks in C2 with overlapped hydrides (stress in Pa)

ductility of hydrogenated zirconium alloys are investigated. The main conclusions can be drawn as follows:

(1) The overall strength and ductility are more sensitive to the cohesive strength of zirconium alloy than that of hydride. Specifically, the increase in the cohesive strength of zirconium alloy promotes the inhibition on the damage evolution, while the increase in that of hydride has slight effects.

(2) The interface has prominent effects on the overall fracture behavior. When the interfacial cohesive strength and fracture energy are lower (interface I), only debonding occurs. When they are the same as the cohesive strength and fracture energy of the hydride (interface II), the fracture occurs at both the hydride and interface. When they are higher (interface III and IV), fracture initiates in the hydride, which is consistent with the experiments.

(3) The geometric characteristics of hydrides play important roles in the overall strength and ductility. Specifically, under the same volume fraction, the coaxial hydrides can lead to an overall strength 13% larger than the uncoaxial ones, and the former can also lead to an overall ductility 62% larger than the latter. The hydride along the tensile direction leads to the much superior overall performance than that perpendicular to it.

Our simulation can effectively expound many fracture phenomena in the experiments of hydrogenated zirconium alloys and also deepen the understanding of the influence of hydrides on their strength and ductility.

Acknowledgements
Not applicable.

Authors' Contributions
CF was in charge of investigation, analysis, and wrote the original manuscript. XG improved the entire analysis and the writing. JL assisted with the analysis and writing. XG and GC supervised the entire investigation. All authors read and approved the final manuscript.

Authors' Information
Chao Fang, born in 1995, received his master degree in mechanics from *Tianjin University, China*, in 2022. He is currently an engineer at *Purification Equipment Research Institute, Handan, China.*
Xiang Guo, born in 1978, is currently an associate professor at *School of Mechanical Engineering, Tianjin University, China*. He received his doctoral degree from *City University of Hong Kong, China*, in 2006. His research interests include fracture and fatigue of engineering materials and structures.
Jianghua Li, born in 1989, is currently a postdoc at *Institute of Mechanics, Chinese Academy of Sciences, China*. She received her doctoral degree from *Tianjin University, China*, in 2020. Her research interests include fatigue and failure mechanism of metal materials.
Gang Chen, born in 1979, is currently a full professor at *School of Chemical Engineering and Technology*, *Tianjin University, China*. He received his doctoral degree from *Tianjin University, China,* in 2005. His research interests include mechanical performance and fatigue behavior of new materials.

Funding
Supported by National Key Research and Development Plan of China (Grant No. 2018YFC0808800), National Natural Science Foundation of China (Grant No. 51875398), and China Postdoctoral Science Foundation (Grant No. 2021M693240).

Availability of Data and Materials
The raw/processed data required to reproduce these findings will be made available upon request.

Declarations

Competing Interests
The authors declare no competing financial interests.

Received: 10 February 2022 Revised: 23 July 2023 Accepted: 27 July 2023
Published online: 17 August 2023

References

[1] V Mallipudi, S Valance, J Bertsch. Meso-scale analysis of the creep behavior of hydrogenated Zircaloy-4. *Mechanics of Materials*, 2012, 51: 15–28.
[2] D F Guo, M Li, Y D Shi, et al. High strength and ductility in multimodal-structured Zr. *Materials and Design*, 2012, 34: 275–278.
[3] M K Khan, M Pathak, S Suman, et al. Burst investigation on zircaloy-4 claddings in inert environment. *Annals of Nuclear Energy*, 2014, 69: 292–300.
[4] T Alam, M K Khan, M Pathak, et al. A review on the clad failure studies. *Nuclear Engineering and Design*, 2011, 241(9): 3658–3677.
[5] G L Liu, C Z Huang, B Zhao, et al. Effect of machined surface integrity on fatigue performance of metal workpiece: A review. *Chinese Journal of Mechanical Engineering*, 2021, 34: 118.
[6] G Sundell, M Thuvander, H O Andren. Barrier oxide chemistry and hydrogen pick-up mechanisms in zirconium alloys. *Corrosion Science*, 2016, 102: 490–502.
[7] H C Chu, S K Wu, R C Kuo. Hydride reorientation in Zircaloy-4 cladding. *Journal of Nuclear Materials*, 2008, 373(1-3): 319–327.
[8] J Tan, S Ying, L Cong, et al. Effect of zirconium hydrides on cyclic deformation behavior of Zr–Sn–Nb alloy. *Scripta Materialia*, 2006, 55(6): 513–516.
[9] G Carpenter. The dilatational misfit of zirconium hydrides precipitated in zirconium. *Journal of Nuclear Materials*, 1973, 48(3): 264–266.
[10] G Domizzi, R A Enrique, J Ovejero-García, et al. Blister growth in zirconium alloys: Experimentation and modeling. *Journal of Nuclear Materials*, 1996, 229: 36–47.
[11] Y S Kim, W E Wang, D R Olander, et al. High-pressure hydriding of Zircaloy. *Journal of Nuclear Materials*, 1996, 240(1): 27–31.
[12] F Long, D Kerr, G Domizzi, et al. Microstructure characterization of a hydride blister in Zircaloy-4 by EBSD and TEM. *Acta Materialia*, 2017, 129: 450–461.
[13] R Dutton, K Nuttall, M P Puls, et al. Mechanisms of hydrogen induced delayed cracking in hydride forming materials. *Metallurgical Transactions A*, 1977, 8(10): 1553–1562.
[14] S Suman, M K Khan, M Pathak, et al. Hydrogen in Zircaloy: Mechanism and its impacts. *International Journal of Hydrogen Energy*, 2015, 40(17): 5976–5994.
[15] S V Ivanova. Hydrogen effected defects evolution in zirconium items of light-water reactors. *International Journal of Hydrogen Energy*, 2006, 31(2): 295–300.
[16] J S Kim, T H Kim, D H Kook, et al. Effects of hydride morphology on the embrittlement of Zircaloy-4 cladding. *Journal of Nuclear Materials*, 2015, 456: 235–245.
[17] Y Zhang, L You, X W Li, et al. In-situ investigation of the fatigue crack initiation and propagation behavior of Zircaloy-4 with different hydrogen contents at RT and 300°C. *Journal of Nuclear Materials*, 2020, 532: 152065.
[18] C C Tseng, M H Sun, C K Chao. Hydride effect on crack instability of Zircaloy cladding. *Nuclear Engineering and Design*, 2014, 270: 427–435.
[19] C Fang, X Guo, G J Weng, et al. Simulation of ductile fracture of zirconium alloys based on triaxiality dependent cohesive zone model. *Acta Mechanica*, 2021, 232: 3723–3736.
[20] W Chen, H Kou, L Chen, et al. Theory model combined with XFEM of threshold stress intensity factor and critical hydride length for delay hydride cracking. *International Journal of Hydrogen Energy*, 2019, 44(54): 29047–29056.

[21] S S Ghorashi, N Valizadeh, S Mohammadi. Extended isogeometric analysis for simulation of stationary and propagating cracks. *International Journal for Numerical Methods in Engineering*, 2012, 89(9): 1069–1101.
[22] N Nguyen-Thanh, K Zhou. Extended isogeometric analysis based on PHT-splines for crack propagation near inclusions. *International Journal for Numerical Methods in Engineering*, 2017, 112: 1777–1800.
[23] X Guo, G Yang, G J Weng, et al. Interface effects on the strength and ductility of bimodal nanostructured metals. *Acta Mechanica*, 2018, 229(8): 3475–3487.
[24] X Guo, Y Liu, G J Weng, et al. Microstructure-property relations in the tensile behavior of bimodal nanostructured metals. *Advanced Engineering Materials*, 2020, 22(6): 2000097.
[25] H T Liu, J Lin, Y Z Sun, et al. Micro model of carbon fiber/cyanate ester composites and analysis of machining damage mechanism. *Chinese Journal of Mechanical Engineering*, 2019, 32: 52.
[26] J H Song, H W Wang, T Belytschko. A comparative study on finite element methods for dynamic fracture. *Computational Mechanics*, 2008, 42: 239–250.
[27] T B Guo, F Zhang, W W Ding, et al. Effect of micro-scale Y addition on the fracture properties of Al–Cu–Mn alloy. *Chinese Journal of Mechanical Engineering*, 2018, 31: 79.
[28] P D Babu, P Gouthaman, P Marimuthu. Effect of heat sink and cooling mediums on ferrite austenite ratio and distortion in laser welding of duplex stainless steel 2205. *Chinese Journal of Mechanical Engineering*, 2019, 32: 50.
[29] Y Peng, C Y Liu, N N Wang. Effect of deformation on microstructure and mechanical properties of medium carbon steel during heat treatment process. *Chinese Journal of Mechanical Engineering*, 2021, 34: 113.
[30] ABAQUS. ABAQUS Theory Manual and User's Manual, version 6.11, Dassault, 2014.
[31] C Z Liu, G P Li, L H Chu, et al. Texture and yielding anisotropy of Zircaloy-4 alloy cladding tube produced by cold Pilger rolling and annealing. *Materials Science & Engineering A*, 2018, 719: 147–154.
[32] G Chen, X Zhang, D K Xu, et al. Multiaxial ratcheting behavior of zirconium alloy tubes under combined cyclic axial load and internal pressure. *Journal of Nuclear Materials*, 2017, 489: 99–108.
[33] K L Murty, M D Mathew. Nondestructive monitoring of structural materials using automated ball indentation (ABI) technique. *Nuclear Engineering and Design*, 2004, 228(1-3): 81–96.
[34] K F Nilsson, N Jakšić, V Vokál, et al. An elasto-plastic fracture mechanics based model for assessment of hydride embrittlement in zircaloy cladding tubes. *Journal of Nuclear Materials*, 2010, 396: 71–85.
[35] S S Kulkarni, V Gupta, D Senor, et al. A microstructure-based modeling approach to predict the mechanical properties of Zr alloy with hydride precipitates. *Computational Materials Science*, 2021, 197: 110654.
[36] Q H Meng, Y Gao, X H Shi, et al. Three-dimensional crack bridging model of biological materials with twisted Bouligand structures. *Journal of the Mechanics and Physics of Solids*, 2022, 159: 104729.
[37] Y Yan, Z L Zhao, X Q Feng, et al. Nacre's brick-mortar structure suppresses the adverse effect of microstructural randomness. *Journal of the Mechanics and Physics of Solids*, 2022, 159: 104769.
[38] M J Wen, H Li, D Yu, et al. Uniaxial ratcheting behavior of Zircaloy-4 tubes at room temperature. *Materials & Design*, 2013, 46: 426–434.
[39] J Xu, S Q Shi. Investigation of mechanical properties of ε-zirconium hydride using micro- and nano-indentation techniques. *Journal of Nuclear Materials*, 2004, 327(2): 165–170.
[40] H Chan, S G Roberts, J Gong. Micro-scale fracture experiments on zirconium hydrides and phase boundaries. *Journal of Nuclear Materials*, 2016, 475: 105–112.
[41] J H Li, Z Y Wang, Y Cheng, et al. Effect of hydride precipitation on the fatigue cracking behavior in a zirconium alloy cladding tube. *International Journal of Fatigue*, 2019, 129: 105230.
[42] S Y Wang, F Giuliani, T B Britton. Slip-hydride interactions in Zircaloy-4: Multiscale mechanical testing and characterization. *Acta Materialia*, 2020, 200: 537–550.
[43] Q D Ouyang, A K Soh, G J Weng, et al. The limit velocity and limit displacement of nanotwin-strengthened metals under ballistic impact. *Acta Mechanica*, 2018, 229: 1741–1757.
[44] X Guo, G Y Chai, G J Weng, et al. Tuning the strength-ductility synergy of nanograined Cu through nanotwin volume fraction. *Computational Materials Science*, 2022, 203: 111073.
[45] S Suman, M K Khan, M Pathak, et al. Effects of δ-hydride precipitated at a crack tip on crack instability in Zircaloy-4. *International Journal of Energy Research*, 2018, 42: 284–292.
[46] M Maric, R Thomas, J Nunez-Iglesias, et al. A novel method for radial hydride analysis in zirconium alloys: HAPPy. *Journal of Nuclear Materials*, 2022, 559: 153442.
[47] S J Min, M S Kim, K T Kim. Cooling rate- and hydrogen content-dependent hydride reorientation and mechanical property degradation of Zr–Nb alloy claddings. *Journal of Nuclear Materials*, 2013, 441(1-3): 306–314.
[48] A S Pierre-Clément, F Cailon, L Q Chen, et al. Quantifying the effect of hydride microstructure on zirconium alloys embrittlement using image analysis. *Journal of Nuclear Materials*, 2021, 547: 152817.